Chapter 5

Resonator design

1 Description of the resonator and the detection scheme

Figure 5.1 shows a resonator that we propose to use for NMR study of nanoscale samples. The design has a spin sample placed between magnetic cylinders, with the sample enclosed by a silicon "paddle" which separates the two cylinders. Torsional motion of the beam causes the magnetic "sandwich" to rotate, and a transverse field at right angles to the beam develops as a result of the rotation. Since the sample rotates with the sandwich, there is no relative motion between the spins and the magnetic cylinders. The field at the spins changes as the resonator moves, however, and so the spins are coupled to the mechanical coordinate.

The mechanical resonator can be used to polarize spins and detect their spectrum at low temperatures. Between transients, the resonator induces longitudinal spin relaxation. At mK temperatures, the spin-lattice interactions which restore the spins to thermal equilibrium between transients become "frozen out," and the time constant T_1 for relaxation to equilibrium increases by orders of magnitude over the room temperature value. Slow relaxation of the spins to thermal equilibrium translates to a pathologically long delay between transients, which makes acquisition of many transients impractical. Resonator-induced longitudinal relaxation replaces spin-lattice relaxation as a means of restoring the spin system to equilibrium between

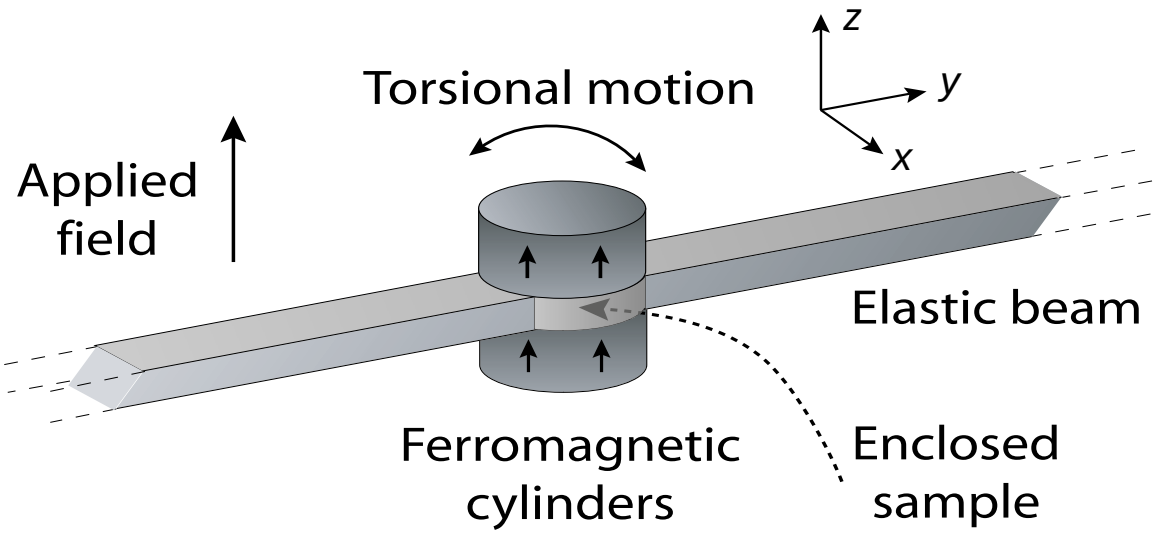

Figure 5.1: Torsional resonator for force-detected NMR spectroscopy. The sample is "sandwiched" between ferromagnetic cylinders, and it rotates with the sandwich about the axis of the torsional beam. The transverse spin dipole couples to the mechanical coordinate through the oscillating transverse field generated by the rotating sandwich.

transients.

In addition to inducing longitudinal relaxation, the resonator can be used to detect the NMR spectrum. The BOOMERANG scheme for force-detected NMR spectroscopy [2, 13, 21, 22] detects a single point of the free-induction decay for each measured transient. In this scheme, a conventional NMR pulse sequence is applied to the spins, and the spins then precess freely for a period of time without being coupled to the resonator. At time t_1 during the FID, a component $\langle I_x(t_1)\rangle$ of the sample's transverse spin is measured by using this component to drive the mechanical resonator. For the resonator shown in figure 5.1, this scheme could be realized by moving the Larmor frequency out of resonance with the mechanical frequency during the NMR pulse sequence and the period of free spin precession, and then performing a $\pi/2$ pulse to store $\langle I_x(t_1)\rangle$ along z while the Larmor frequency is brought back into resonance with the mechanical frequency. An additional $\pi/2$ pulse returns $\langle I_x(t_1)\rangle$ to the transverse plane, at which point it is spin-locked. The spin-locked transverse dipole exerts a driving force on the mechanical resonator, and the resulting mechan-

ical motion is detected. Analysis of the mechanical motion yields a measurement of $\langle I_x(t_1)\rangle$. By repeating the measurement for a range of values t_1, a record of the spins' time evolution is obtained, and Fourier analysis yields an NMR spectrum.

This measurement scheme extracts information by analyzing the mechanical response to torques exerted by the spin sample. It is therefore essential that the applied radiofrequency (RF) field not drive the resonator during the spin-locking. This goal can be achieved by applying the RF in pulses along the length of the torsion beam. A magnetic field directed along the length of the beam does not drive the torsional motion, so an ideal applied field would drive only the spins without imparting motion to the resonator. If imperfections in the fabricated structures cause the resonator to be driven by the applied RF, the mechanical response to the spins can be separated from the mechanical response to the applied RF by applying the spin-locking field in pulses. Between pulses, excitation which has been imparted to the resonator by the applied field will decay quickly on the time scale required for decay of the precessing transverse spin dipole. After the excitation due to the applied field has decayed, the mechanical motion observed up to the beginning of the next RF pulse will be due to driving by the spins. (Pulsed spin-locking of a solid sample is discussed in reference [26].)

Detection of the torsional motion might be accomplished by means of a single-electron transistor (SET). A scheme for SET detection of translational mechanical motion has been demonstrated experimentally at a level of sensitivity near the quantum limit [25]. Mechanical motion changes the state of the SET by modulating the gate capacitance. This scheme might be adapted for the detection of torsional motion by capacitively coupling electrodes to the magnetic sandwich, with the coupling designed in such a way that the capacitance is modulated by the mechanical motion.

The resonator design shown in figure 5.1 can be modified for purposes of magnetic resonance imaging. Figure 5.2 shows a resonator design which is appropriate for imaging a small sample. The sample is placed a hole in the silicon paddle, and the gradient created by the magnetic cylinder selects a resonant section of the sample for imaging. Scanning the applied field shifts the position of the resonant section being

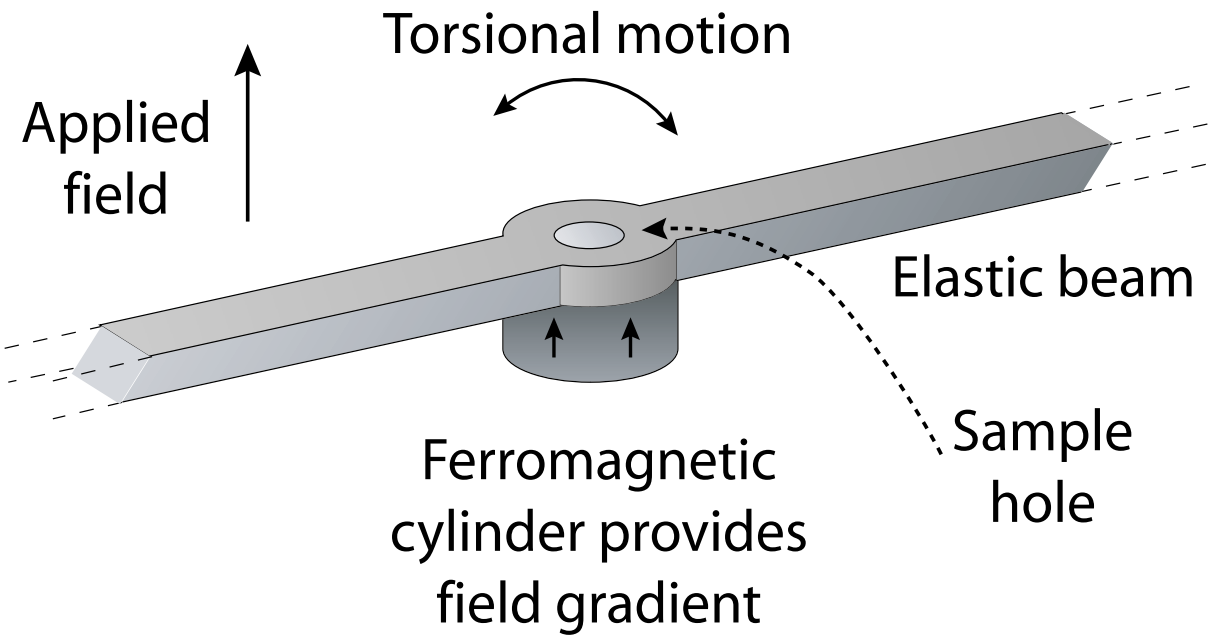

Figure 5.2: Torsional resonator for force-detected NMR imaging. The cylinder creates a field gradient which selects a resonant slice of the sample for imaging, and the transverse spin dipole couples to the mechanical coordinate through the oscillating transverse field generated by the moving cylinder.

detected and allows imaging of the sample.

2 Selection of the resonator design

The resonator design shown in figure 5.1 was selected after alternative designs were considered. Three types of mechanical motion were considered: 1) Radial motion of a magnet along a line connecting the magnet to the spins, 2) Horizontal motion of a magnet placed above the spins, and 3) Rotation of a hollow magnet or an array of magnets around an axis passing through the spins. The figure of merit used to compare different designs was the magnitude of the coupling constant g defined by equation (2.9). Since the rate constant for longitudinal relaxation of a single spin is

$$\begin{aligned} R_h &= 2g^2\tau_h\left(n_{\mathrm{th}}+1\right) \\ &\propto g^2, \end{aligned}$$

the magnitude of g characterizes the efficiency with which a particular form of mechanical motion can cool spins. We found that the cooling efficiency of these three types of motion was similar, with the magnitude of g varying by a factor of order unity between resonator designs.

The choice to use a torsional resonator was motivated by the fact that spins can be coupled to torsional mechanical motion without the need for relative motion between the sample and nearby magnets. Surface friction between nearby moving parts can decrease cooling efficiency as well as detection sensitivity, since damping decreases the magnitude of the mechanical response to forces or torques exerted by the spins. Relative motion between the sample and nearby moving parts is unavoidable if the mechanical motion is translational, but it can be eliminated by the use of a torsional resonator. This can be seen by noting first that the spins drive the resonator only if mechanical motion modulates the interaction between the spins and moving magnets. If both the sample and the magnets move in unison along a straight line, with no relative motion occurring between sample and magnets, the spin-magnet interactions are not modulated by the motion. By way of contrast, consider an idealized example in which an array of magnets creates a uniform field at the spin sample. If both the magnets and the sample are rotated together, with no relative motion occurring between sample and magnets, the spins experience a rotating field, and the interaction between the spin degrees of freedom and the magnet array is modulated as the array rotates. Use of a torsional resonator therefore eliminates the need for relative motion between the sample and nearby moving magnets.

Two types of torsional resonators were considered. In addition to the design shown in figure 5.1, we studied a design in which the sample is placed at the center of a short magnetic tube, with the axis of the tube aligned with the applied field. The tube's axis rotates out of alignment with the applied field as the resonator moves out of equilibrium position. The design of figure 5.1 was selected instead in order to create a more homogeneous field at the spins.

Our initial estimates of g were based on a simplified model in which the ferromagnetization of the resonator rotates with the resonator itself, regardless of the

magnitude of the static applied field. Calculations of g based on this model suggested that for the size scale at which efficient cooling might be achieved, nanoscale mechanical resonators would have frequencies corresponding to the Larmor frequency of hydrogen in a large applied field. Since a large applied field would tend to keep the ferromagnetization aligned with the applied field rather than rotating with the resonator, the simplified model we were using was of doubtful validity in the regime of interest, and we considered instead a model in which the magnetization remains continually aligned with the applied field as the resonator moves. As discussed in section 5.1, we found that the strength of the spin-resonator coupling was increased by the switch from a model which assumed infinitely hard magnetic materials to a model which assumed soft magnetic materials. Section 4 discusses the validity of our assumption that the magnetization remains aligned with the applied field as the resonator moves.

3 Condition for resonance between the spins and the resonator

Efficient energy transfer from spin to resonator can only occur if the precession frequency of the spins is resonant with the mechanical frequency. In deriving the interaction Hamiltonian in section 1 of chapter 2, the resonance condition was expressed as

$$\omega_0 = -\omega_h, \tag{5.1}$$

since ω_h is positive by definition, and since

$$\omega_0 = -\gamma B_z$$

is negative in the common case where $\mathbf{B}$ is parallel to the positive z-axis yields and γ is positive. Note, however, that the sign of $-\gamma B_z$ depends on the choice of coordinate axes; if the coordinate axes are rotated so that the z-axis is directed opposite $\mathbf{B}$, the

sign of $-\gamma B_z$ changes, while the physical resonance between spins and mechanical oscillator is unchanged. It follows that the resonance condition could be written as

$$\omega_0 = \pm\omega_h, \tag{5.2}$$

with the sign determined by the choice of reference frames rather than by the physical nature of the problem.

In designing a device for which spin precession is resonant with mechanical motion, we express (5.2) as

$$\omega_0^2 = \omega_h^2, \tag{5.3}$$

or equivalently

$$\gamma^2 B_z^2 = \frac{k_h}{I_h}, \tag{5.4}$$

where k_h and I_h are the respective spring constant and moment of inertia. If the mechanical energy and the energy of the electromagnetic field energy both vary as the resonator moves, then the k_h and I_h will each include a contribution associated with the electromagnetic field as well as a contribution associated with the mechanical motion. Appendix J shows by means of a numerical example that the contribution to I_h associated with the electromagnetic field is negligible. An expression for the electromagnetic contribution to k_h is derived in Appendix K. This contribution is determined by the dependence of magnetostatic energy U_{mag} on the resonator's coordinate, where

$$U_{\text{mag}} = -\mu \cdot \mathbf{B}_a - \frac{1}{2}\int \mathbf{M} \cdot \mathbf{B}_h \, d^3x. \tag{5.5}$$

In (5.5), $\mathbf{B}_a$ is the applied field, $\mathbf{B}_h$ is the resonator's magnetic field, and $\mathbf{M}$, μ are its respective magnetization and dipole moment. The magnetic spring constant k_{mag} is given by

$$k_{\text{mag}} = \frac{d^2 U_{\text{mag}}}{d\theta^2}. \tag{5.6}$$

In general, both terms on the right side of (5.5) can contribute to k_{mag}, but simplifications are possible in two limiting cases. For a sufficiently hard magnetic

material or a sufficiently weak applied field, $\mathbf{M}$ remains constant within a reference frame fixed in the resonator. In this case, the second term on the right side of (5.5) does not depend on the resonator coordinate θ and may be dropped for purposes of finding k_{mag}. If the applied field lies along the positive or negative z-axis and the dependence of μ_z on θ is given by

$$\mu_z(\theta) = \mu_z \cos\theta,$$

equation (5.6) becomes

$$k_{\mathrm{mag}} = \mu_z B_{a,z}. \tag{5.7}$$

In the opposite limit, the applied field is sufficiently large that μ remains aligned with $\mathbf{B}_a$ as the resonator moves, and it is the second term of (5.5) which determines k_{mag}, since $\mu \cdot \mathbf{B}_a$ is constant. In this limit, k_{mag} is a constant which does not depend on the exact value of B_a:

$$k_{\mathrm{mag}} = \frac{d^2}{d\theta^2}\left\{-\frac{1}{2}\int \mathbf{M}\cdot\mathbf{B}_h\, d^3x\right\}. \tag{5.8}$$

The resonance condition (5.4) can be written in the form

$$\gamma^2 \left|\mathbf{B}_a + \mathbf{B}_h\right|^2 = \frac{k_{\mathrm{beam}} + k_{\mathrm{mag}}}{I_h}, \tag{5.9}$$

where k_{beam} is the spring constant of the elastic suspension. The applied field may be considered the variable determined by the solution of this equation. In evaluating resonator designs, we used (5.7) or (5.8) as the magnetic spring constant. Finite-element software (Maxwell 3D v11, Ansoft Corporation, Pittsburgh) was used to compute the magnetic spring constant given by (5.8).

In general, equation (5.9) has more than one solution. If the magnetic spring constant is given by (5.7), for instance, there are always two solutions to (5.9). In the examples we considered, one of the solutions corresponded to an applied field which was sufficiently large that protons at 10 mK would be highly polarized in the

field. We used this solution in our initial comparison of different resonator designs.

4 Model of the resonator's magnetization

The resonator was modelled as having uniform magnetization $\mathbf{M}$ which remains continually aligned with the applied field $\mathbf{B}_a$. In this section we justify that approximation using analytic expressions for the demagnetizing field which is present within uniformly-magnetized spheroids of soft magnetic material. In keeping with our use of the notation $\mathbf{B}_h$ for the resonator's field, we also will use $\mathbf{B}_h$ to denote the field of a given spheroid.

4.1 Uniform magnetization

The field $\mathbf{B}_h$ within a uniformly-magnetized spheroid is itself uniform and is given by [27]

$$\mathbf{B}_h = -\mu_0 \left(N_a M_x, N_a M_y, N_c M_z\right) + \mu_0 \mathbf{M}. \tag{5.10}$$

Here the x-axis, y-axis, and z-axis coincide with the spheroid axes of length a, a, and c, respectively, and N_a, N_c are constants which depend only on the ratio $r = c/a$ [27]. In the limiting case where $r \to 0$ (thin disc), we have

$$N_a \to 0,$$
$$N_c \to 1,$$

while in the case $r \to \infty$ (long rod), we have

$$N_a \to 1/2,$$
$$N_c \to 0.$$

Equation (5.5) gives the magnetostatic energy U_{mag} of the spheroid:

$$U_{\text{mag}} = -\mu \cdot \mathbf{B}_a - \frac{1}{2}\int \mathbf{M} \cdot \mathbf{B}_h \, d^3x.$$

Consider the problem of finding the shape which minimizes the magnetostatic energy of a spheroid of a given volume and magnetization in the absence of an applied field. From (5.10), we have

$$U_{\text{mag}} = -\frac{1}{2}\mu_0 \int \mathbf{M} \cdot \mathbf{M} \, d^3x + \frac{1}{2}\mu_0 \int \left(N_a M_x^2 + N_a M_y^2 + N_c M_z^2\right) \, d^3x,$$

and since the constants N_a, N_c are nonnegative,

$$U_{\text{mag}} \geq -\frac{1}{2}\mu_0 \int \mathbf{M} \cdot \mathbf{M} \, d^3x.$$

The minimum magnetostatic energy

$$U_{\text{min}} = -\frac{1}{2}\mu_0 \int \mathbf{M} \cdot \mathbf{M} \, d^3x$$

is achieved, for instance, in the limiting case of a arbitrarily long, thin rod, with $\mathbf{M}$ lying along the axis of the rod. We can use U_{min} as an estimate of the minimum magnetostatic energy which can be achieved by a given volume of magnetization $\mathbf{M}$. The term $-\mu_0 \left(N_a M_x, N_a M_y, N_c M_z\right)$ appearing in (5.10) can be considered a "demagnetizing field," since it raises the energy of a uniformly-magnetized structure above U_{min} and introduces the possibility that the low-energy configuration of $\mathbf{M}$ may be nonuniform.

The field required to saturate a magnet to a state of uniform magnetization is often characterized in terms of the demagnetizing field which exists within the magnet [27]. If the magnetization is nonuniform due to demagnetizing fields within the magnet, application of an external field stronger than the demagnetizing fields is expected to saturate the magnet [27]. Since the demagnetizing field within the ferromagnetic

cylinders of the mechanical resonator is at most of order

$$\mu_0 M \leq 2\,\mathrm{T}\,,$$

it is reasonable to model the mechanical resonator's magnetization as uniform when the applied field is of order 10 T or more, as in the examples we have considered.

Even in the absence of an applied field, exchange interactions will produce uniform magnetization in a sufficiently small particle. Since exchange energy is increased when $\mathbf{M}$ varies over small distances within a magnet, the exchange energy associated with variation in $\mathbf{M}$ across a nanoscale magnet eventually becomes larger than the magnetostatic energy associated with uniform magnetization [28], with the result that the low-size limit for multidomain particles is in the range 20-800 nm [29]. Both the dimensions of the resonator's ferromagnetic cylinders and the magnitude of the applied field suggest that the magnetization should be modelled as uniform.

4.2 Magnetization constant in the lab frame

In addition to considering the resonator's magnetization to be uniform, we model it as remaining continually aligned with the applied field. The error associated with this simplifying assumption can be estimated by using equations (5.10) and (5.5) to estimate the angle by which $\mathbf{M}$ would rotate away from $\mathbf{B}_a$ during the mechanical motion. As in section 4.1, we consider a uniformly magnetized spheroid for which the x-axis, y-axis, and z-axis coincide with the spheroid axes of length a, a, and c. The applied field $\mathbf{B}_a$ lies in the xz-plane at an angle θ from the z-axis. Let ϕ denote the angle between $\mathbf{M}$ and the z-axis when $\mathbf{M}$ is oriented so as to minimize magnetostatic energy. We wish to derive an expression for $\phi\,(\theta)$, the angle by which the magnetization rotates away from the spheroid z-axis when the applied field is rotated through angle θ.

We can find ϕ by minimizing the energy U_{mag} given by equation (5.10), or equiv-

alently, by minimizing U_{mag}/V, where V is the volume of the spheroid:

$$\frac{U_{\text{mag}}}{V} = -\mathbf{M}\cdot\mathbf{B}_a - \frac{1}{2}\mathbf{M}\cdot\mathbf{B}_h.$$

Since the demagnetizing H-field is given by

$$\begin{aligned}\mathbf{H}_d &= -\left(N_a M_x, 0, N_c M_z\right)\\ &= -\left(N_a M\sin\phi, 0, N_c M\cos\phi\right),\end{aligned}$$

we have

$$\mathbf{B}_h = \mu_0 M\left((1-N_a)\sin\phi, 0, (1-N_c)\cos\phi\right)$$

and

$$-\frac{1}{2}\mathbf{M}\cdot\mathbf{B}_h = \frac{1}{2}\mu_0 M^2\left[(N_a - N_c)\sin^2\phi + (N_c - 1)\right].$$

The angle between $\mathbf{M}$ and $\mathbf{B}_a$ has magnitude $|\theta-\phi|$, and so

$$\mathbf{M}\cdot\mathbf{B}_a = MB_a\cos\left(\theta-\phi\right).$$

Dropping from the expression for E/V any terms which do not vary with ϕ, we obtain

$$U_{\text{mag}}/V = \frac{1}{2}\mu_0 M^2\left(N_a - N_c\right)\sin^2\phi - MB_a\cos\left(\theta-\phi\right).$$

Making the definition

$$K_u \equiv \frac{1}{2}\mu_0 M^2\left(N_a - N_c\right)$$

allows us to write the energy density as

$$U_{\text{mag}}/V = K_u\sin^2\phi - MB_a\cos\left(\theta-\phi\right). \tag{5.11}$$

Stationary points occur when

$$0 = \frac{\partial}{\partial\phi}\left(U_{\text{mag}}/V\right) = 2K_u\sin\phi\cos\phi - MB_a\sin\left(\theta-\phi\right). \tag{5.12}$$

We can consider the equation

$$2K_u \sin\phi\cos\phi = MB_a \sin(\theta - \phi)$$

to define $\phi(\theta)$, and implicit differentiation can be used to derive a series expression for $\phi(\theta)$. Defining

$$A = \frac{2K_u}{MB_a},$$

we find that the first and second derivatives of ϕ evaluated at $\theta = 0$ are

$$\begin{aligned} \phi'(0) &= \frac{1}{A+1}, \\ \phi''(0) &= 0. \end{aligned} \tag{5.13}$$

The second order Taylor series for $\phi(\theta)$ is

$$\phi(\theta) \approx \frac{\theta}{A+1}. \tag{5.14}$$

In the case where $M = 2.3\,\mathrm{T}/\mu_0$ and $B_a = 15\,\mathrm{T}$, with the ratio of spheroid axes $r = c/a$ of order 2, for instance, equation (5.14) predicts that $\mathbf{M}$ rotates away from the applied field through an angle roughly 5% of the angle θ between the spheroid and $\mathbf{B}_a$.

The calculations we have presented do not include dynamic effects: the magnet is held motionless in a static field, and the low-energy orientation of $\mathbf{M}$ is found. In reality, the orientation of the applied field (as seen from a reference frame fixed in the magnet) will be changing at a frequency on the order of 500 MHz. However, simple estimates can be used to show that in this range of frequencies, the problem of finding the state of the magnetization can be treated as a static one. In investigating dynamic effects on the evolution of $\mathbf{M}$, we consider a lab frame which has the z-axis aligned with the field. Within this reference frame, each ferromagnetic dipole experiences a static applied field and a varying field due to the changing orientation of the resonator. A first correction to the model in which all fields are static can be

made by supposing that ferromagnetic dipoles experiences a static field along z and a transverse field oscillating at around 500 MHz. We can estimate the importance of dynamic effects by comparing the AC susceptibility of the particle at this frequency to the DC susceptibility. This model problem is equivalent to experiments done in studying ferromagnetic resonance (FMR), and results from the literature of this field show that the resonator's AC susceptibility at this frequency is very close to its DC susceptibility. Ferromagnetic resonance peaks occur in a higher range of frequencies than NMR peaks, due to the larger gyromagnetic ratio of the electron, and the linewidths observed in FMR experiments are typically only a small fraction of the resonance frequency [30]. Frequencies of $\sim$ 500 MHz are far enough from FMR resonance frequencies that the AC susceptibility of the resonator's ferromagnetic cylinders can be considered equal to the DC susceptibility in this frequency range.

5 Strength of the spin-resonator coupling

5.1 Effect of soft magnetic material on the coupling strength

Figure 5.3 shows the configuration of $\mathbf{M}$ in the resonator's ferromagnetic cylinders when the "sandwich" shown in figure 5.1 has rotated through a substantial angle. The angle of rotation is highly exaggerated in order to highlight the difference between the configurations for hard and soft magnetic materials. Hard magnetization rotates with the cylinders, while soft magnetization remains aligned vertically with the field. Examination of this figure might initially suggest that the spin-resonator coupling, which is proportional to the transverse field linear in θ, will be weak if soft magnetic materials are used, since it might appear that a larger transverse field will develop if the magnetization rotates with the cylinders.

Finite-element simulations have shown, however, that the soft oscillator in figure 5.3 has the larger transverse field. A rationalization for this result can be seen in figure 5.4. The magnetization in the soft magnetic material can be expressed as the sum of two components, one parallel to the cylinder axis and one perpendicular to

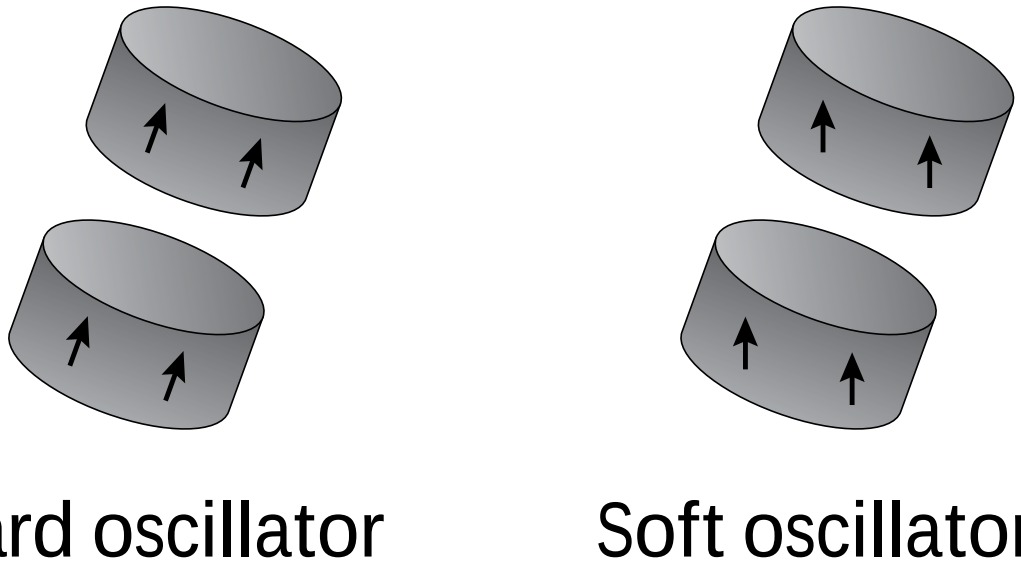

Figure 5.3: Comparison of magnetization orientation for hard and soft magnetic materials. The ferromagnetic cylinders are those of the oscillator in figure 5.1 after it has rotated through a substantial angle about its torsional axis. The orientation of the cylinder magnetization for hard and soft magnetic materials is shown.

it. The fields generated by these two components add constructively at the location of the spins. The field generated by each of the components can be rationalized by replacing each of the four cylinders on the right side of the figure by a single dipole which has the same orientation as the cylinder's magnetization. The field lines of these dipoles give a qualitative estimate of the contribution that each cylinder makes to the field at the center of the sandwich.

The ideas expressed in figure 5.4 can be demonstrated analytically if the cylinders in the figure are replaced by two identical spheroids (either prolate or oblate). Suppose that the sandwich has rotated through an angle θ away from the vertical applied field $\mathbf{B}_a$. If the magnetization M remains aligned with $\mathbf{B}_a$, then we can consider the resonator field at the spins to be the superposition of two fields, one generated by magnetization $M\cos\theta$ aligned along the sandwich axis, and the other generated by magnetization $M\sin\theta$ aligned at right angles to the axis. Reference [31] gives analytic expressions for the fields external to uniformly magnetized ellipsoids, and it can be shown that that the magnetization aligned with the sandwich axis generates

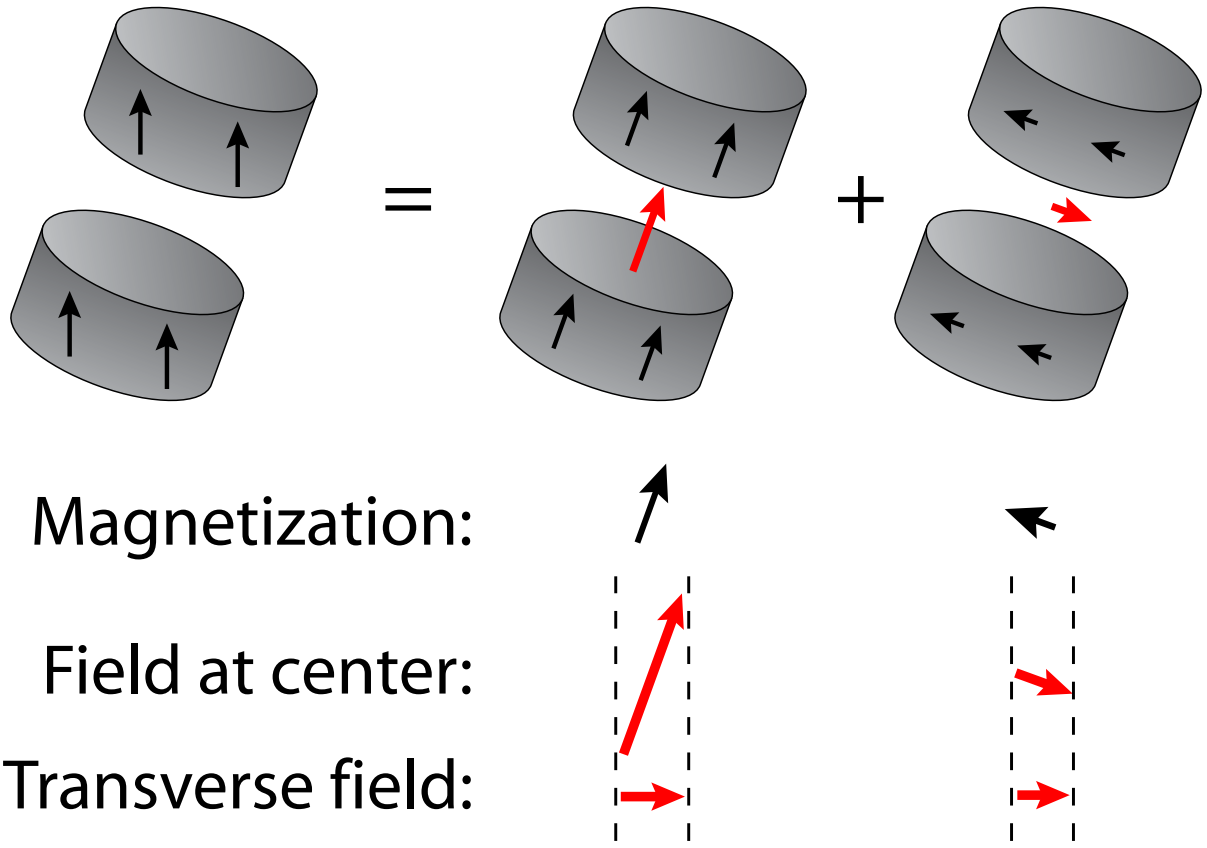

Figure 5.4: Comparison of the transverse field for hard and soft magnetic materials. The ferromagnetic cylinders are those of the oscillator in figure 5.1. In the case where the cylinders are composed of soft magnetic material, the transverse field which couples to the nuclear spins can be expressed as the sum of two components that add constructively. If the cylinders are composed of hard magnetic materials, only the first of these components is present. As a result, soft magnetic materials yield a strong coupling to the spins.

at the spins a field $\mathbf{B}_1$ parallel to itself, while the magnetization at right angles to the resonator axis generates a field $\mathbf{B}_2$ antiparallel to itself. Expressed in the unrotated Cartesian components of the lab frame, these two fields are

$$\mathbf{B}_1 = B_h \cos\theta \left(\sin\theta, 0, \cos\theta\right),$$
$$\mathbf{B}_2 = \frac{1}{2} \sin\theta \left(\cos\theta, 0, -\sin\theta\right).$$

From these formulas we obtain

$$\frac{dB_x}{d\theta} = \frac{3B_h}{2} \cos 2\theta$$

and

$$\frac{d^2 B_z}{d\theta^2} = -3B_h \cos 2\theta.$$

Evaluating at $\theta = 0$ gives

$$\frac{dB_x}{d\theta} = \frac{3B_h}{2}, \tag{5.15}$$
$$\frac{d^2 B_z}{d\theta^2} = -3B_h. \tag{5.16}$$

By way of contrast, a magnetically hard sandwich would have

$$B_x\left(\theta\right) = B_h \sin\theta,$$
$$B_z\left(\theta\right) = B_h \cos\theta,$$

as well as

$$\frac{dB_x}{d\theta} = B_h,$$
$$\frac{d^2 B_z}{d\theta^2} = -B_h$$

at $\theta = 0$. We see that switching from an ideal magnetically hard resonator to an ideal magnetically soft resonator increases the magnitude of $dB_x/d\theta$ by a factor of

3/2, and the magnitude of $d^2B_z/d\theta^2$ by a factor of 3. The factor of 3/2 in (5.15) is due to the fact that the contribution to $dB_x/d\theta$ made by $\mathbf{B}_2$ is half the size of the contribution made by $\mathbf{B}_1$.

The data from finite-element simulations is consistent with the hypothesis that (5.15) and (5.16) continue to be valid for the configuration of soft magnets shown in figure 5.3, which contains two cylinders rather than two spheroids. The finite-element software package Maxwell 3D v11 (Ansoft Corporation, Pittsburgh) was used to calculate $B_x(\theta)$ and $B_z(\theta)$ after rotating the sandwich axis away from the applied field up to 5° in steps of 1°, and curve-fitting was used to estimate $dB_x/d\theta$ and $d^2B_z/d\theta^2$. These calculations were done for each sandwich geometry tested during the optimization described in section 6, and for geometries in which cylinders of diameter 100 nm and height 50 nm were separated by distances ranging from 5 nm to 50 nm. For each geometry that was simulated, the data points for $B_x(\theta)$ lay essentially on a straight line, and the value of $dB_x/d\theta$ obtained by curve fitting was within about 1% of the computed value of $3B_h/2$. Substantial random residuals were seen when quadratic curves were fitted to computed plots of $B_z(\theta)$ in order to estimate $d^2B_z/d\theta^2$, which may be used to rationalize the fact that computed values of $d^2B_z/d\theta^2$ differed from $-3B_h$ by up to 15%. Adopting the hypothesis that (5.15) and (5.16) are valid for resonators of the type shown in figure 5.1 allows us to express the field $\mathbf{B}(\theta)$ to second order in θ as

$$\mathbf{B}(\theta) = \mathbf{B}_a + B_h\left(\frac{3}{2}\theta, 0, 1-3\theta^2\right).$$

5.2 Upper bound on the torque between the spins and the resonator

Since detection sensitivity is enhanced if the torque acting between spins and resonator is increased, an estimated upper bound on the attainable torque per spin is helpful in evaluating resonator designs. A simple estimate can be made using the model introduced in section 5.1, which replaces the resonator's two cylinders with

spheroids. Since the strength of the spin-resonator torque is given by

$$G = \mu_x \, dB_x/d\theta,$$

it follows from equation (5.15) that largest possible torque will be obtained when $dB_x/d\theta$ reaches its maximal value.

The formulas given in reference [31] can be used to express G in the form

$$G/\mu_x = \mu_0 M V K_{\text{geom}},$$

where V is the volume of the magnetic material, and K_{geom} depends on the shape of the spheroids as well as the distance between them. Given the constraints that M and V are fixed, and that a gap must exist between the two spheroids, the maximal value of G/μ_x can be found by optimizing K_{geom}. We found that G/μ_x achieves its maximal value in the limiting case where the spheroids become arbitrarily long and thin. The maximal value is independent of the volume of the spheroids and is given by

$$(G/\mu_x)_{\max} = 3\mu_0 M. \tag{5.17}$$

For the example resonator presented in table 5.3 of section 6, the value of $\mu_0 M$ is 2.3 T, and the limiting value of G/μ_x is 7 T, which is larger by a factor of 4 than the value calculated for the resonator.

Note that when the spheroids are nearly touching, the dependence of G/μ_x on shape anisotropy of the spheroids is weak. If the spheroids are prolate, and if the long axis of each is just twice the length of the short axes, for instance, the value of G/μ_x is 83% of the limiting value given by (5.17) when the separation between spheroids is negligible. Even in the case where the shape anisotropy is zero and the resonator is composed of two spheres separated by a negligible gap, we have G/μ_x equal to 67% of the upper limit.

6 Optimization of example resonators

Two different optimizations of the magnetic "sandwich" shown in figure 5.1 were performed. For the first optimization, the separation S between the ferromagnetic cylinders and the diameter D of the sandwich were constrained by

$$S \geq 50\,\mathrm{nm}\,, \tag{5.18}$$

$$D \geq 100\,\mathrm{nm}\,, \tag{5.19}$$

and for the second optimization, S and D were constrained by

$$S \geq 25\,\mathrm{nm}\,, \tag{5.20}$$

$$D \geq 50\,\mathrm{nm}\,. \tag{5.21}$$

Both optimizations had the same constraints on the width w and thickness t of the rectangular cross-section of the torsional beam:

$$w \geq 50\,\mathrm{nm}\,,$$

$$t \geq 50\,\mathrm{nm}\,,$$

and the silicon paddle separating the two ferromagnetic cylinders was constrained to have the same diameter as the cylinders. The resonator's ringdown time was fixed at $\tau_h = 6\,\mu\mathrm{s}$ during the optimizations.

In characterizing the sensitivity associated with a particular choice of dimensions for the magnetic sandwich, the beam dimensions which maximize the SNR formula (4.50) were found, where the decay time of the spin-locked signal was fixed at 1 s. This optimization was performed before we had investigated the way in which resonator-induced relaxation affects the lifetime of a spin-locked signal. For all of the resonators we considered, the time-constant $2/R_h$ for resonator-induced decay of the spin-locked signal was greater than 1 s. Our optimization can therefore be considered to incorporate an assumption that factors other than resonator-induced relaxation limit

the period of time during which spin-locking can be performed. Since (4.51) shows that SNR is independent of all resonator parameters other than ω_h/T_h in an ideal spin-locking field, an alternative approach to designing the resonator would be to minimize acquisition time using expressions given in section 7 of chapter 4.

The optimal beam must have

$$w = t = 50\,\mathrm{nm}\,.$$

This can be seen by noting that, given a resonator of frequency ω_h and a beam with width or thickness greater than 50 nm, we could decrease the beam's moment of inertia without changing ω_h by switching to a shorter beam that has a 50 nm $\times$50 nm cross-section; this decrease in the moment of inertia would increase the resonator's sensitivity. The optimization of beam dimensions for a given magnetic sandwich therefore involved varying the beam length l in steps of 100 nm to find the optimal frequency ω_h. The applied field B_a was then chosen to satisfy the resonance condition determined by beam length.

In performing the optimizations, we assumed a sample consisting of a single spin 1/2. As a result, the instrument noise characterized by $S_{\mathrm{inst}}(\omega)$ was substantially larger than the spin noise. The optimal geometry of the magnetic sandwich was not sensitive to the changes in A_{det}. The same geometry was obtained when the motion detection was assumed to be quantum-limited or to have a noise temperature $T_N = 18T_{QL}$. (The quantum-limited noise temperature T_{QL} is discussed in section 4.3 of chapter 4.)

Sensitivity is in general optimal when the cylinders are as close together as possible. Decreasing the separation between the magnets improves SNR in two ways: 1) The resonator's moment of inertia is decreased, which decreases $S_{\mathrm{inst}}(\omega)$, and 2) The field B_h at the center of the sandwich is increased, which increases the size of the torque acting between spins and resonator, since this torque is proportional to

$$\frac{dB_x}{d\theta} = \frac{3}{2}B_h. \tag{5.22}$$

Length L	Diameter D	Beam length	Single-shot SNR	$1/R_h$	B_a
35 nm	100 nm	1600 nm	0.109	3.6 s	14 T

Table 5.1: Selected parameters for a resonator optimized with a separation of 50 nm between magnetic cylinders.

Length L	Diameter D	Beam length	Single-shot SNR	$1/R_h$	B_a
40 nm	55 nm	2200 nm	0.236	0.91 s	20 T

Table 5.2: Selected parameters for a resonator optimized with a separation of 25 nm between magnetic cylinders.

(Equation (5.22) is explained in section 5.1.) It was this observation which motivated us to perform optimizations with different constraints on the separation S. The optimal designs associated with the different constraints (5.18) and (5.20) were found by varying the diameter D and the length L of each ferromagnetic cylinder in steps of 5 nm, while keeping the separation S between them fixed at the minimum value. The two dimensions D and L were varied until the SNR given by (4.50) reached its maximum value. For each choice of cylinder dimensions, the Maxwell 3D v11 software package (Ansoft Corporation, Pittsburgh) was used to calculate B_h and $dB_x/d\theta$. Magnetic spring constants were not calculated, since initial numerical tests found the magnetic spring constant to be negligible compared to the elastic spring constant.

Tables 5.1 and 5.2 show the results of the two optimizations. The values of single-shot SNR assume detection of a single spin which has been cooled by the resonator to a temperature of 10 mK. Quantum-limited motion detection is included in the estimate by setting

$$A_{\text{det}} = 1/2.$$

For each of these designs, SNR changes by less than 1% in response to a change of 5 nm in L or D within the constraints set by (5.18) through (5.21). Note that constraint (5.21) may be considered superfluous, since the optimal design in table 5.2 is not limited by this constraint.

A modified version of the resonator presented in table 5.2 will be used for numerical

examples. The applied field of 20 T can be reduced without significantly changing the resonator's sensitivity. We modified the design by lowering the applied field and simultaneously increasing the beam length until SNR has decreased by 5% from the optimal value given in table 5.2. This procedure yields an applied field of 14 T and a beam length of 3.5 μm for the example resonator. Tables 5.3 and 5.4 give additional details regarding the resonator. In table 5.4, equation (4.50) is used to calculate the the SNR for detecting $\langle I_x(t_1)\rangle$ at an instant when

$$\langle I_x(t_1)\rangle = \frac{PN}{2}.$$

In evaluating SNR, we use the assumption

$$T_{1\rho} = 1\,\mathrm{s}$$

which defined the optimization. The alternative assumption that resonator-induced relaxation is responsible for decay of the spin-locked signal would yield

$$T_{1\rho} = 2/R_h = 1.5\,\mathrm{s}\,.$$

Note that the entry "N at spin-noise limit" in table 5.4 gives the number of spins N at which the spin noise equals the instrument noise. This number is a natural measure of the instrument noise associated with the resonator, since instrument noise becomes dominant as the number of spins is decreased below this number. Note as well that the volume 4.4 nm^3 in table 5.3 represents a cylinder of diameter 2 nm and height 1.4 nm within which the field of the magnetic sandwich differs by no more than 25 kHz from the field B_h at the center of the sandwich. An ice sample filling this volume would contain ~ 300 protons. Note that this sample is sufficiently small to satisfy the condition that guarantees that oscillatory energy exchange between spins and resonator will be suppressed. Since the number of thermal quanta $n_{\mathrm{th}} \ll 1$, we

Magnet length L	$40\,\mathrm{nm}$
Magnet diameter D	$55\,\mathrm{nm}$
Separation S between magnets	$25\,\mathrm{nm}$
Magnetization $\mathbf{M}$	$2.3\,\mathrm{T}\,/\mu_0$
Magnet density	$7900\,\mathrm{kg}\,/\,\mathrm{m}^3$
Beam cross-section	$50\,\mathrm{nm} \times 50\,\mathrm{nm}$
Beam length	$3.5\,\mu\mathrm{m}$
Beam stiffness constant C_{44}	$7.96 \times 10^{10}\,\mathrm{N}\,/\,\mathrm{m}^2$
Density of beam and paddle	$2.33 \times 10^3\,\mathrm{kg}\,/\,\mathrm{m}^3$
Sandwich moment of inertia	$2.1 \times 10^{-33}\,\mathrm{kg\,m}^2$
Beam moment of inertia	$4.2 \times 10^{-33}\,\mathrm{kg\,m}^2$
Frequency $\omega_h/2\pi$	$628\,\mathrm{MHz}$
Ringdown time τ_h	$6.0\,\mu\mathrm{s}$
Quality factor	$11,800$
Applied field	$13.6\,\mathrm{T}$
Resonator field B_h	$1.1\,\mathrm{T}$
Transverse derivative $dB_x/d\theta$	$1.6\,\mathrm{T}$
Coupling constant g	$313\,\mathrm{s}^{-1}$
Rate constant $1/R_h$	$0.77\,\mathrm{s}$
Sample polarization P	0.91
Volume where $\lvert\Delta\omega\rvert \leq 25\,\mathrm{kHz}$	$4.4\,\mathrm{nm}^3$
Resonator temperature T_h	10 mK
Thermal quanta n_{th}	0.05

Table 5.3: Parameters for the optimized example resonator.

	Quantum limited detection ($T_N = T_{QL}$)	$T_N = 18T_{QL}$
SNR for a single spin	0.224	0.0602
N when $SNR = 1$	6 spins	18 spins
N at spin noise limit	7 spins	112 spins
SNR at spin noise limit	1.2	4.8

Table 5.4: Sensitivity of the optimized example resonator.

can use (2.16) to verify that such oscillations are suppressed:

$$\begin{aligned} g\sqrt{N} &= \left(313\,\mathrm{s}^{-1}\right)\sqrt{300} \\ &\approx 5.4 \times 10^3\,\mathrm{s}^{-1} \\ &\ll 330 \times 10^3\,\mathrm{s}^{-1} \\ &= \frac{2}{\tau_h}. \end{aligned}$$

The frequency offset 25 kHz was chosen based on an estimate that sample spins having a frequency spread of 50 kHz could be rotated uniformly by RF pulses. Note that line broadening proportional to the field inhomogeneity across the sample can be eliminated, for example, by the use of pulse sequences which select zero-quantum coherences or multiquantum heteronuclear coherences whose frequency does not shift in response to an offset in a static applied field [32]. Note as well that equation (2.26) implies that spins whose Larmor frequency is out of resonance with ω_h by 25 kHz are cooled more slowly by the resonator between transients. An offset of

$$\beta = 2\pi \times 25\,\mathrm{kHz}$$

from resonance decreases the cooling rate by a factor of

$$\frac{1}{1 + (\beta\tau_h)^2} \approx 0.5.$$

7 Use of non-metallic magnetic material

A requirement of the scheme we have proposed is that the mechanical resonator be exposed to RF magnetic fields during the NMR pulse sequence as well as during spin-locking. If the ferromagnetic material of the cylinders is metallic, eddy currents will be induced in the metallic cylinders by the RF fields. Appendix M presents an example which illustrates the way in which the resulting temperature change ΔT_h is determined by physical parameters which depend strongly on the dimensions and

temperature of the resonator. Estimates of the order of magnitude of these parameters based on the limited information available in the literature leave open the possibility that the temperature change ΔT_h could substantially decrease detection sensitivity if conducting ferromagnetic materials are used.

A possible solution to the problem of eddy-current heating is the use of dielectric material as the source of the resonator's field. A natural candidate for such a material would be an insulator that contains magnetic ions. Even if the material is paramagnetic rather than ferromagnetic, magnetic ions would remain aligned with the applied field at low temperatures, yielding time-independent magnetization in the lab frame, as in the model discussed in section 4. At fields of order 10 T and mK temperatures, ferromagnetic material is not necessarily a requirement for the resonator design or the numerical examples we have presented.

Ions with partially filled f-orbitals can have relatively large angular momenta, in part due to the fact that the orbital angular momentum of the tightly-bound f-orbitals is not quenched by the crystal field. Lanthanide oxides are natural candidates for non-metallic magnetic materials to be used in force-detected NMR, and EuO is particularly promising, since it has a large saturation magnetization of $2.41\,\mathrm{T}/\mu_0$ at 0 K [33], and since it has been prepared as an epitaxial thin film on Si [34] as well as in the form of nanocrystals [35, 36]. Although the saturation magnetization of the nanocrystals and epitaxial thin films were not measured, the Curie law susceptibility of the nanocrystals showed that each Eu^{2+} ion in these materials has a moment of ~ 7 Bohr magnetons [35, 36], as in the bulk compound [33].

At room temperature EuO is a semiconductor with a resistivity many orders of magnitude larger than that of metals, and the resistivity increases as the temperature is lowered [37]. At temperatures below 77 K, EuO is ferromagnetic [33]. Doping with excess Eu causes a metal-insulator transition to occur around the Curie temperature, but low-temperature bulk resistivities observed by Shapira and coworkers for doped EuO were at least three orders of magnitude larger than the room-temperature conductivity of Fe [38]. Since the power dissipation due to eddy-current heating is inversely proportional to resistivity, the estimate presented in Appendix M suggests

that eddy-current heating should be negligible even for the "metallic" form of doped EuO.